10
Determination of Elastic Strains Using Electron Backscatter Diffraction in the Scanning Electron Microscope

Michael Krause, Matthias Petzold, and Ralf B. Wehrspohn

10.1
Introduction

The understanding and management of stress and strain is of fundamental importance in the design and implementation of novel materials and manufacturing processes in a wide range of applications. While stress due to external loads can be calculated with a certain degree of accuracy, residual stress, which remains in a body that is stationary and at equilibrium with its surroundings, is much more difficult to predict. To date, a large number of residual stress measurement techniques are available. Some of these techniques are destructive, while others can be used without significantly altering the component; some have excellent spatial resolution, whereas others are restricted to near-surface stresses or to specific classes of materials. However, even if these methods, for instance, X-ray diffraction, Raman spectroscopy, or TEM, have proved to provide acceptable measurements of the residual stress in certain cases, there is still a strong demand for alternative techniques that can provide a means of determining local strains with high spatial resolution on the one hand and high strain sensitivity on the other hand.

In this chapter, we will show how electron backscatter diffraction (EBSD) can be used to determine the local state of stress and strain in a region of a material. Developed as an additional characterization technique to a scanning electron microscope (SEM), the technique has passed through various stages of development and has experienced rapid acceptance in research and industry in the past decade. Nowadays, EBSD is most widely used for orientation determination [1–3], discrimination of unknown crystalline phases [4–6] (see also Figure 10.1a), and orientation mapping (Figure 10.1b) on the surfaces of bulk polycrystals. Since this technique is based on recording electron backscatter diffraction patterns (EBSP)[1] that represent all angular relationships in the crystal, it is obvious to use it for the determination of local elastic strains.

---

[1] In literature, the terms "electron backscatter diffraction pattern (EBSP)," "backscatter Kikuchi pattern (BKP)," and "backscatter electron Kikuchi pattern (BEKP)" are often used interchangeably.
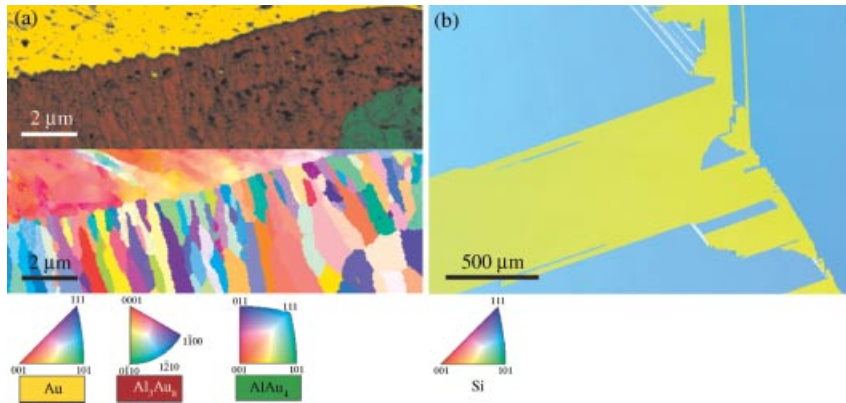
Figure 10.1 (a) EBSD phase map and orientation map (inverse pole figure representation) of intermetallic compounds formed in a gold–aluminum bond wire interconnect measured with a step size of 50 nm; (b) orientation map (inverse pole figure representation) of a polycrystalline Si wafer surface measured with a step size of 5 μm.

10.2
Generation of Electron Backscatter Diffraction Patterns

In order to understand the principles of strain determination using electron backscatter diffraction, it is necessary to model the physical processes that lead to the formation of the characteristic diffraction features: Kikuchi lines and bands. Although the dynamical theory of electron diffraction is needed to explain the exact intensity distribution in an electron backscatter diffraction pattern [7–10], a simplified model based on the kinematic approximation can also be used to explain the geometrical relations in the observed network [11]. This model will be presented briefly.

An EBSP is generated on a detector screen by backscatter diffraction of a stationary beam of high-energy electrons that is focused on a small area of a crystalline solid. As the beam enters the sample, the electrons are subject to a diffuse inelastic scattering in all directions. This means that there must be always some electrons that impinge on a particular set of parallel lattice planes at the Bragg angle θ_B and undergo elastic scattering to give a reinforced beam. Since diffraction of the electrons through the Bragg angle is occurring in all directions, the locus of the diffracted radiation is the surface of two cones that extend symmetric around the normal of the reflecting atomic planes, separated by twice the Bragg angle (Figure 10.2b). If some sort of recording medium is positioned so as to intercept these diffraction cones, a pair of parallel conic sections results in hyperbolas that are essentially seen as two straight parallel lines, known as Kikuchi lines. The distance between a pair of Kikuchi lines is a function of the Bragg angle that is inversely proportional to the interplanar spacing d_{hkl}. The geometry of the EBSP can be interpreted as a gnomonic projection of the
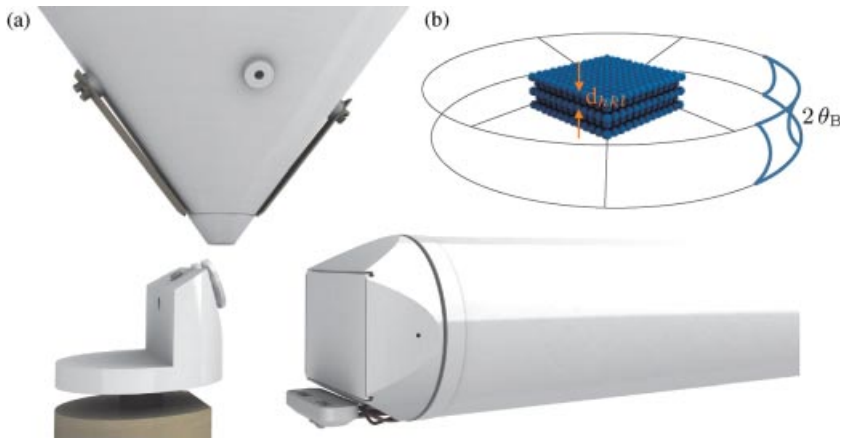
Figure 10.2 (a) Schematic of a typical EBSD setup, showing the pole piece of the SEM, the tilted specimen (in this case, using a pretilted sample holder), and the detector. (b) Diffraction cones with respect to a reflecting plane separated by twice the Bragg angle.

crystal lattice on the flat detector screen with the center of the projection given by the point of impingement of the primary electron beam.

The instrumentation for generating and capturing electron backscatter diffraction patterns usually consists of three main parts: the SEM, the pattern acquisition device, and the software (Figure 10.2a). The EBSP is commonly formed on a transparent phosphor screen (approximately 4 cm in diameter) that is positioned parallel to the primary beam and the tilt axis of the specimen. To enhance the proportion of backscattered electrons that are able to undergo diffraction and to escape from the specimen surface, the sample and the incident electron beam draw an angle of typically 20°. Nowadays, the pattern is recorded through a lead glass window from outside the specimen chamber using a high-sensitivity CCD camera that can produce binned images on the order of 100×100 pixels at a rate of more than 600 images per second. In most EBSD systems, the acquisition device is mounted on a retractable stage. The phosphor screen is generally matched to the spectral response of the CCD sensor and is covered by a thin, conductive coating (aluminum or tin–indium–oxide). This coating enhances the brightness of the phosphor by reflecting light back toward the camera, absorbs low-energy electrons, and reduces charging of the phosphor screen.

10.3
Strain Determination Through Lattice Parameter Measurement

As already mentioned, EBSD is widely used to determine local grain structure and texture of polycrystalline materials. In contrast, elastic strain measurement from EBSD patterns (EBSP) is not yet a standard routine. Nowadays, there is much activity in this area and thus many different approaches to measure elastic strains can be found in the literature. In general, elastic strains can be obtained using two distinct

approaches: the direct measurement of lattice parameters on the one hand and determination of changes in the crystal structure with respect to a known reference position on the other hand.

Due to the comparatively poor angular resolution of typical EBSD systems and the absence of higher-order diffraction lines and the low contrast of the Kikuchi bands, the direct measurement of the Kikuchi bandwidth from EBSPs, in order to determine the lattice plane spacing, cannot attain the precision required to enable strain measurement [12]. Moreover, it has been shown that the determination of changes of interplanar angles, which are of course measured in the conventional automated analysis of EBSD patterns for crystal orientation analysis, would not lead to a sufficient strain sensitivity for the same reasons [12].

To overcome the limitations of strain determination using direct measurement of Kikuchi band position mentioned above, Maurice and Fortunier developed an interesting approach that accounts for the hyperbolic nature of the Kikuchi band edges and thus allows greater precision in locating the bands [13]. They proposed to extend the standard procedure for the detection of Kikuchi bands based on the Hough transform that is widely used in commercial EBSD software to a three-dimensional space using a generalized 3D Hough transform. This transform is obtained from the derivative of an EBSP by taking into account the wave vector of the diffracted electron beam and the reciprocal vector associated with the particular (hkl) plane. By this means, the Bragg angle to which this pixel contributes is calculated and the intensity of each pixel is added to a 3D voxel. The corresponding 3D Hough space has axes composed of the base parameters ϱ and θ, but with an additional ordinate axis proportional to the width of the band, that is, $\sin(\theta)$. Assuming that the crystal orientation is known, a maximum intensity search in fairly small volumes of the 3D Hough space is performed to obtain the three parameters describing the Kikuchi line hyperbola and thus its exact position. In a proof of concept, the authors demonstrated a strain sensitivity of 2×10^{-4} in case of geometrically calculated diffraction patterns. In general, the band detection accuracy is impaired by image distortions due to the camera optics and accurate knowledge of the position of the point source is required. Even if no measurements on real patterns are reported so far, the methodology shows promise though a reduction in strain sensitivity due to intensity asymmetries across the bands could be expected.

10.4
Strain Determination Through Pattern Shift Measurement

10.4.1
Linking Pattern Shifts to Strain

Beside attempts to detect intense elastic strain gradients through a blurring of the EBSD patterns [14, 15], strain measurement using the cross-correlation-based pattern shift analysis could be seen as the most mature one. Introduced by Troost *et al.* [16] and Wilkinson *et al.* [17], the approach relies on the fact that elastic strains and small rotations cause small shifts in features within the Kikuchi patterns. These
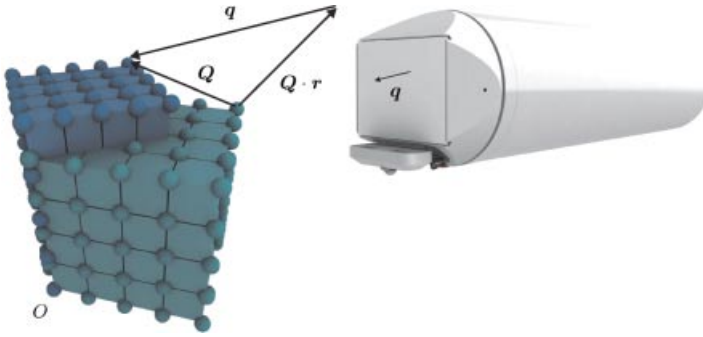
Figure 10.3 Schematic showing how a strain and a rotation in the crystal lattice can be related to a shift of an EBSD pattern on the detector screen (reference crystal: cubic; strained crystal: tetragonal distorted and rotated).

shifts can be measured using cross-correlation techniques and be related to the strain and the rotation tensor. Due to its high application potential, this methodology will be described in the following section in detail.

The general principles of strain analysis using the "pattern shift" approach are as follows: One pattern from the series to be analyzed is chosen as a reference pattern, whereas this reference pattern should come from a point on the sample for which the strain is known or is assumed to be zero. A set of square subsections is defined across the patterns and shifts relative to positions in the reference pattern are determined for all the subsections/patterns in the series using 2D cross-correlation functions. To link the measured pattern shifts to the present strain state, Wilkinson *et al.* [18] used the displacement gradient tensor $A = \nabla u$ describing the deformation mapping r onto r' (Figure 10.3) so that

$$r' = Ar \tag{10.1}$$

(u-displacement at position x). The displacement of the crystal lattice Q caused by strain and rotation is related to A by

$$Q = r' - r = (A - I)r \tag{10.2}$$

(I is unit matrix). Considering the fact that EBSD measures only the projection of Q perpendicular to r denoted by q, it follows

$$q = Q - \lambda r = [A - (\lambda + 1)I]r \tag{10.3}$$

(λ is unknown scalar). Measurement of q for a given r gives three equations from which λ can be eliminated. Expanding and transposing Eq. (10.3) yields the following two simultaneous equations:

$$
r_1 r_3 \left[\frac{\partial u_1}{\partial x_1} - \frac{\partial u_3}{\partial x_3} \right] + r_2 r_3 \frac{\partial u_1}{\partial x_2} + r_3^2 \frac{\partial u_1}{\partial x_3} - r_1^2 \frac{\partial u_3}{\partial x_1} - r_1 r_2 \frac{\partial u_3}{\partial x_2} = r_3 q_1 - r_1 q_3
$$

$$
r_2 r_3 \left[\frac{\partial u_2}{\partial x_2} - \frac{\partial u_3}{\partial x_3} \right] + r_1 r_3 \frac{\partial u_2}{\partial x_1} + r_3^2 \frac{\partial u_2}{\partial x_3} - r_1 r_2 \frac{\partial u_3}{\partial x_1} - r_2^2 \frac{\partial u_3}{\partial x_2} = r_3 q_2 - r_2 q_3
$$

$$\tag{10.4}$$

Measuring q for four widely spaced directions r allows an exact solution to be determined for the system of linear equations, giving eight of the nine degrees of freedom within the gradient displacement tensor A. The remaining ninth degree corresponds to hydrostatic dilatation that cannot be obtained using this method since a simple change in the widths of Kikuchi bands generates no change in the interplanar angles and thus does not cause any shift of a pattern feature in the EBSP. In order to improve the statistic of shift measurement for each pattern, shifts could be measured at more than four positions. Then, accordingly overdetermined system of equations has to be solved for an approximate solution in a least square of error sense.

The last degree of freedom can be determined by imposing the conditions of a plane stress. Due to the fact that EBSPs are generated very close to the surface of a sample, it is reasonable to assume that the normal stress σ_{33} perpendicular to the free surface approximates to zero [19]. We can write

$$\sigma_{33} = 0 = C_{33kl}\varepsilon_{kl} \tag{10.5}$$

where C_{ijkl} are the elastic constants referred to the sample axis system. By this means, an additional equation is available allowing separation of all three normal strains.

Since the displacement gradient tensor A contains information about strains *and* rotations, it has to be decomposed into a symmetric part and an antisymmetric part using the transpose of A denoted by A^T. It follows

$$A = \frac{1}{2}(A + A^T) + \frac{1}{2}(A - A^T) = \varepsilon + \omega \tag{10.6}$$

Thus, we can describe strain by

$$\varepsilon = \begin{bmatrix} \varepsilon_{11} & \varepsilon_{12} & \varepsilon_{13} \\ \varepsilon_{12} & \varepsilon_{22} & \varepsilon_{23} \\ \varepsilon_{13} & \varepsilon_{23} & \varepsilon_{33} \end{bmatrix} = \begin{bmatrix} \dfrac{\partial u_1}{\partial x_1} & \dfrac{1}{2}\left(\dfrac{\partial u_1}{\partial x_2} + \dfrac{\partial u_2}{\partial x_1}\right) & \dfrac{1}{2}\left(\dfrac{\partial u_1}{\partial x_3} + \dfrac{\partial u_3}{\partial x_1}\right) \\ \dfrac{1}{2}\left(\dfrac{\partial u_1}{\partial x_2} + \dfrac{\partial u_2}{\partial x_1}\right) & \dfrac{\partial u_2}{\partial x_2} & \dfrac{1}{2}\left(\dfrac{\partial u_2}{\partial x_3} + \dfrac{\partial u_3}{\partial x_2}\right) \\ \dfrac{1}{2}\left(\dfrac{\partial u_1}{\partial x_3} + \dfrac{\partial u_3}{\partial x_1}\right) & \dfrac{1}{2}\left(\dfrac{\partial u_2}{\partial x_3} + \dfrac{\partial u_3}{\partial x_2}\right) & \dfrac{\partial u_3}{\partial x_3} \end{bmatrix}$$

while the lattice rotation can be described using the rotation tensor

$$\omega = \begin{bmatrix} 0 & \omega_{12} & \omega_{13} \\ -\omega_{12} & 0 & \omega_{23} \\ -\omega_{13} & -\omega_{23} & 0 \end{bmatrix} = \begin{bmatrix} 0 & \dfrac{1}{2}\left(\dfrac{\partial u_1}{\partial x_2} - \dfrac{\partial u_2}{\partial x_1}\right) & \dfrac{1}{2}\left(\dfrac{\partial u_1}{\partial x_3} - \dfrac{\partial u_3}{\partial x_1}\right) \\ \dfrac{1}{2}\left(\dfrac{\partial u_2}{\partial x_1} - \dfrac{\partial u_1}{\partial x_2}\right) & 0 & \dfrac{1}{2}\left(\dfrac{\partial u_2}{\partial x_3} - \dfrac{\partial u_3}{\partial x_2}\right) \\ \dfrac{1}{2}\left(\dfrac{\partial u_3}{\partial x_1} - \dfrac{\partial u_1}{\partial x_3}\right) & \dfrac{1}{2}\left(\dfrac{\partial u_3}{\partial x_2} + \dfrac{\partial u_2}{\partial x_3}\right) & 0 \end{bmatrix}$$

10.4.2
Measurement of Pattern Shifts

Detecting the shift of a digital image or certain features in a series of similar images is a well-studied topic. Among all the different methods that could be found in literature, cross correlation and phase correlation are the conventionally used criteria.

The use of cross correlation for template matching is motivated by the distance measure (squared Euclidean distance)

$$d_E^2(r,s) = \sum_{(i,j) \in R} (I(r+i,s+j) - R(i,j))^2 \tag{10.7}$$

($R(u,v)$, reference image; (r,s), shift of the reference image; and $I(u,v)$, arbitrary gray scale image). In order to determine the best match between $I(u,v)$ and $R(u,v)$, it is sufficient to minimize $d_E^2(r,s)$ that can be written as

$$d_E^2(r,s) = \underbrace{\sum_{(i,j) \in R} (I(r+i,s+j) - R(i,j))^2}_{A(r,s)}$$
$$+ \underbrace{\sum_{(i,j) \in R} (R(i,j))^2}_{B=\text{constant}} - 2 \underbrace{\sum_{(i,j) \in R} I(r+i,s+j) \cdot R(i,j)}_{C(r,s)} \tag{10.8}$$

If the term $A(r,s)$ is approximately constant, the remaining cross-correlation term is a measure of the similarity between the image and the reference image:

$$C(r,s) = \sum_{(i,j) \in R} I(r+i,s+j) R(i,j) \tag{10.9}$$

The computation of this cross correlation can be performed either in original space or in Fourier space utilizing

$$(f * g)(u,v) := \sum_{\xi=0}^{M-1} \sum_{\eta=0}^{N-1} = f(\xi,\eta) g(\xi-u,\eta-v) \tag{10.10}$$

Thus, the cross-correlation coefficient can be calculated efficiently using the fast Fourier transform $\mathcal{F}$ by

$$C = \mathcal{F}^{-1}[\mathcal{F}(f)\mathcal{F}^*(g)] \tag{10.11}$$

($\mathcal{F}^*$ indicates the complex conjugate of the Fourier transform). The peak intensity in the resulting cross-correlation image is located at a position described by the vector $\boldsymbol{q}$ that describes how features contained in one image shift, compared to another image that also contains those features. If the cross-correlation function is computed directly from two pictures, it is possible to determine the shift level only with

resolution on whole pixels. If higher (subpixel) resolution is required, it is necessary to use interpolation [20].

There are several disadvantages that have to be considered if Eq. (10.9) is used for template matching:

- If $A(r,s)$ varies with position, matching can fail if the correlation between the feature and an exactly matching region in the image is less than the correlation between the feature and a bright spot.
- The range of $C(r,s)$ depends on the size of the feature.
- Equation (10.9) is not invariant to changes in image amplitude such as those caused by changing lighting conditions across the image sequence.

The shift of pattern features relative to the pattern from the reference position is typically measured at numerous widely spaced subregions at exactly the same place in the CCD camera image. Figure 10.4 outlines the main steps in the image processing procedure used to determine the small displacements within the pattern. To avoid any leakage problems during the fast Fourier transform, the mean intensity of each subregion is subtracted from every pixel and a window function (i.e., Hanning, Gauss, or $\sin^2$) is applied to bring the edge values of each subregion smoothly to zero. The resulting image is then passed through a bandpass filter to sharpen the edges of the Kikuchi bands on the one hand and to remove noise on the other hand.

In order to estimate the strain sensitivity of the "pattern shift" approach, different methodologies can be found. The first estimation of strain sensitivity has been given by Wilkinson who quoted a measurement repeatability of 2×10^{-4} in case of pattern shifts induced during beam shift and sample rotation experiments conducted on unstrained high-quality single crystal samples. These results have been in good accordance with measurements conducted on strained SiGe epilayers, where a standard deviation of 2.5×10^{-4} was found for each component of the gradient displacement tensor. One of the most comprehensive works regarding the attainable accuracy of strain measure-
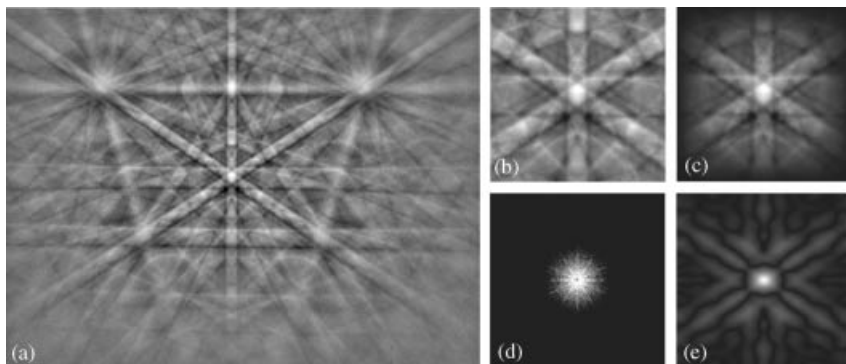

Figure 10.4 (a) EBSD pattern from a silicon single crystal; (b) subregion centered on a certain pattern feature (i.e., zone axis); (c) edge values of each ROI are progressively brought to zero using a weighting function; (d) Fourier transform of the subregion; (e) cross-correlation with the ROI from the reference pattern.
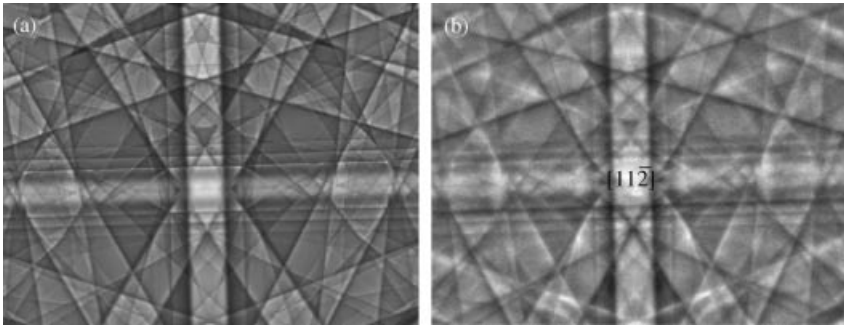
Figure 10.5 Dynamical electron diffraction simulations (a) and experimental narrow-angle EBSD pattern (b) of a Si(100) sample at 20 kV.

ment using EBSD has been presented by Villert *et al.* [21], who measured the difference between applied and measured values of the displacement gradient tensor in case of geometrically simulated diffraction patterns. There, he indicated an accuracy better than 10^{-4} for applied strains of 2×10^{-3} if a cross-correlation error of 0.05 pixel is guaranteed. More recently published paper [22, 23], which confirm previous results, demonstrated the potential of using dynamical, simulated electron backscatter diffraction patterns in order to estimate the possible strain sensitivity and possible influencing factors. Using dynamical simulated diffraction patterns almost any phase, orientation, EBSD geometry, and lattice distortion can be simulated, whereas extremely fine structures can be observed that are often blurred in experimental diffraction patterns (Figure 10.5). However, due to the potentially much higher image quality compared to real EBSPs, accuracy assessment based on such patterns can be seen as a measure of the lower limit of strain sensitivity.

10.5
Sampling Strategies: Sources of Errors

Modern EBSD systems generally offer two different computer-controlled sampling modes to collect diffraction patterns from individual points, linescans, or grids of points. Depending upon the type of analysis, EBSPs can be recorded using either control of the electron beam, in which the focused primary bean is moved across the stationary specimen surface, or by translating the specimen mechanically under the focused stationary electron beam, usually named as stage scan mode. The last mentioned scan method enables the accommodation of large measurement fields, only limited in size by the range of travel of the specimen stage, whereas the step size calibration is independent of the SEM magnification. In contrast, digital beam scanning offers an extremely high speed and precision in beam positioning. However, the diffraction geometry and thus pattern center position, specimen to screen distance as well as background intensity and focus settings will vary from point to point due to the tilted specimen surface and beam deflection.

The sensitivity of the strain measurement results to calibration parameters (i.e., pattern center position and specimen-to-screen distance) has been examined by several authors [21, 22, 24, 25]. It has been shown that a precise knowledge of the source point position is not necessary to realize an accurate strain measurement if EBSPs from reference and strained material were obtained with the same projection parameters. This is of course the case only if EBSD scans are made using the stage scan mode on a perfectly flat specimen or if the change in projection parameters between individual points is well known. In the last case, the EBSD system has to be calibrated dynamically from spot to spot that is typically made by scanning the electron beam across a larger field on a single crystal and measuring the inherent shift of the EBSD pattern across the phosphor screen. Subsequently, the measured shifts of pattern features caused by strains and rotations can be separated from artificial shifts due to the projection parameter variations by simple subtraction. However, due to the small size of subsections that are used to measure the shift between two patterns, this procedure is applicable only up to a certain degree of beam deflection. Otherwise, unequal Fourier spectra will be analyzed during template matching and the cross correlation will fail.

Additional errors could arise from defects in the phosphor screen. Also, pollution that cannot be removed from the screen would cause fixed features in exactly the same position for each pattern and could lead to artifacts in the analysis of the corresponding pattern shifts. In order to reduce the effect of these features, Wilkinson *et al.* [25] proposed the use of standard background correction and filtering in the frequency domain. Even if this approach is very useful to remove random noise and differences in background intensities from patterns, its effect on distinct defects and pollution is rather small. In fact, it is possible to consider these artifacts by capturing a background image and applying a dynamic background correction and stretching to it. The resulting image will be characterized by a widely homogeneous distribution of gray scale values over the entire image and small black features resulting from imperfections on the screen. This image can be analyzed through binarization by setting a threshold to a certain gray scale value and classifying all pixels with values above this threshold as white and all other pixels as black (Figure 10.6). By carefully adjusting this threshold and applying appropriate neighborhood criteria, imperfections of the screen can be detected. Hence, subregions containing imperfections of a certain size that could be defined by the operator could be excluded from the analysis also in automated processing procedures.

10.6
Resolution Considerations

One of the most attractive features of electron backscatter diffraction is its unique capability to perform rapid, automated diffraction analysis of crystalline materials with excellent spatial resolution. The attainable resolution in general is a function of the density and constitution of the material, the acceleration voltage of the primary electrons, the beam profile, the specimen tilt, and the software used for pattern
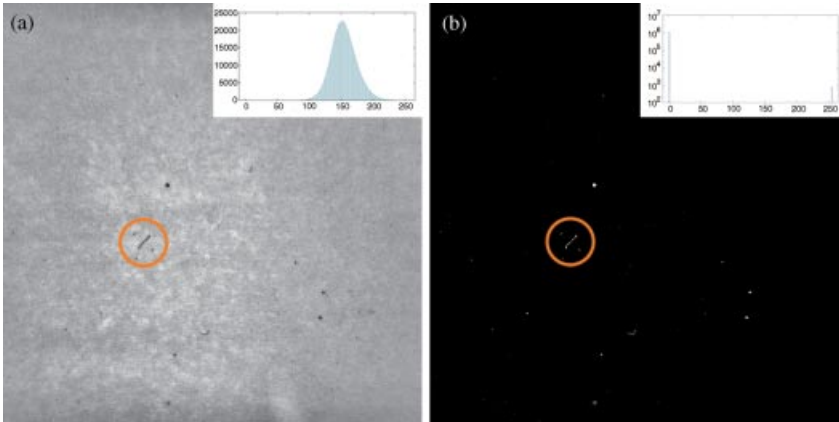
Figure 10.6 (a) Filtered background image showing small black features resulting from imperfections on the screen and (b) corresponding binarized image.

analysis [26]. In particular, the highly tilted specimen geometry has important implications both for EBSD spatial resolution and for the surface sensitivity. In fact, due to the specimen tilt, the interaction volume for backscattered electrons is asymmetric along the beam direction. Consequently, the resolution needs to be defined with respect to three orthogonal directions: lateral resolution (within the specimen plane but normal to the beam direction), longitudinal resolution (within the specimen plane but parallel to the beam direction) that is typically three times the value of the lateral resolution and depth resolution (extent of depth information). To date, two different definitions of spatial resolution could be found in literature: the *physical* resolution that indicates how far away from a large-angle grain diffracted intensities from both crystals can be obtained and the *effective* resolution that is a measure of how accurate an orientation microscopy system may resolve a large-angle grain boundary using software algorithms to deconvolute overlapping patterns. Usually, the effective resolution is better than the physical. However, in case of strain determination using the "pattern shift" approach, the latter is the significant one. The lateral resolution is usually measured by carrying out small scan steps across a boundary standing perpendicular to the sample tilt axis and determining the distance over which patterns cannot be solved. In order to determine the lateral physical resolution for silicon, a string ribbon wafer surface with a large-angle grain boundary standing perpendicular to the surface has been analyzed (Figure 10.7). The beam was moved in steps of 10 nm toward the grain boundary and a diffraction pattern was taken at every position. The first weak Kikuchi bands of the second crystal became visible at (50 ± 10) nm away from the boundary that is synonymic for the physical resolution.

The depth of the surface layer that gives rise to an EBSP can be determined by applying layers of amorphous metal to the surface of a Si single crystal and measuring the EBSD pattern quality in dependence of coating thickness [27]. In the present
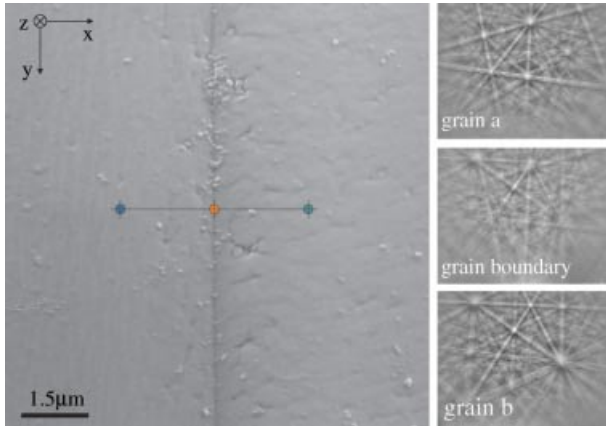
Figure 10.7 SE image of a large-angle grain boundary used to determine the physical lateral resolution in case of silicon (measurements have been performed under conditions where the lateral resolution measured in an SE image is on the order of the beam diameter). The resolution is defined as follows: *x*, lateral resolution; *y*, longitudinal resolution; and *z*, depth resolution.

study, the sensitivity of EBSD patterns to coating thickness has been explored by coating silicon with platinum thin films of known thickness ranging from 1 to 8 nm. Figure 10.8 outlines the pattern quality in dependence of coating thickness, expressed using a quality parameter proposed by Krieger Lassen *et al.* [28]. The results show an almost exponential decrease in pattern quality that is detectable for each acceleration voltage. As shown in Figure 10.8, reducing acceleration voltage
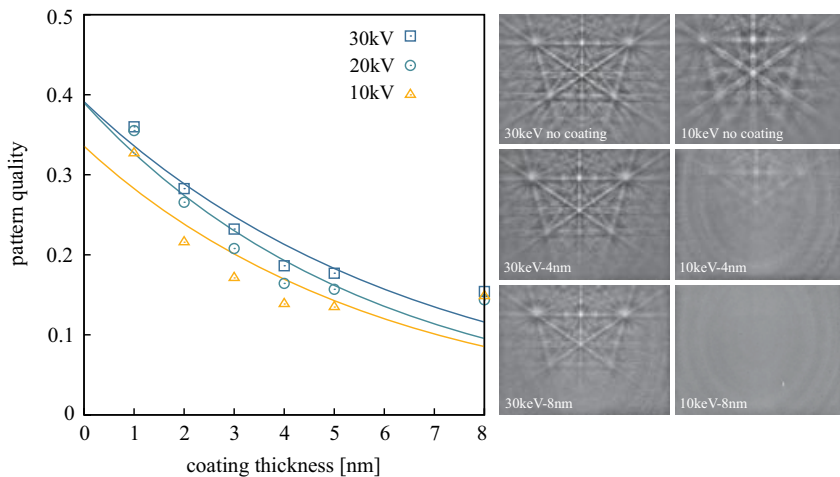

Figure 10.8 Pattern quality of EBSPs obtained from a silicon crystal that has been sputter-coated with differently thick layers of amorphous platinum in dependence of coating thickness.

leads to less beam penetration and thus blurred patterns from the underlying silicon compared to higher primary beam energies. The exact value of depth resolution depends on its definition. If we define the depth resolution as the coating thickness where 50% of the original intensity is left, we obtain a value of ~4 nm for all three electron energies. This result seems to be inconsistent with the visual impression (Figure 10.8). However, one has to consider that pattern quality parameters are strongly affected by a variety of factors, so that the absolute values of pattern quality cannot be compared unambiguously. For instance, changes in experimental parameters such as acceleration voltage, beam current, and exposure time of the CCD camera will strongly influence the degradation of the patterns and thus the numerical value of the pattern quality. In the present study, the lower penetration depth in case of a 10 keV beam energy results in a premature saturation of the quality parameter that is the reason for the almost similar depth resolution compared to higher beam energies.

10.7
Illustrative Application

Several researchers successfully used electron backscatter diffraction patterns to investigate both elastic strain fields in multilayer compound semiconductor systems [14, 15] and lattice curvature in metallic materials [19, 25, 29, 30]. Indeed, most of the quantitative EBSD strain measurements have been realized on epitaxially grown $Si_{1-x}Ge_x$ layers on silicon substrates [16, 17, 21].

Utilizing the cross correlation-based "pattern shift" methodology, the need of an unstrained reference position seems to be a clear limitation. According to this, most of the semiconductor systems investigated so far could be considered to be model systems that have been chemically patterned to provide zones where the silicon is accessible and thus reference EBSD patterns of unstrained material could be obtained. However, there is a multitude of possible applications far beyond academic research, in particular in the field of semiconductor technologies, where such a reference position could be found. In fact, the need for experimental methods that gain access to these positions could be seen to be the bigger challenge. In the following section, we will give an example application of how low-energy focused ion beams can be used in order to provide unstrained reference positions in *strained Silicon-on-Insulator* (sSOI) layers and consequently how EBSD can be used to determine the elastic strain and rotation tensors of these nanosized single-crystal films.

SOI technology offers CMOS performance enhancement with the use of an embedded oxide layer to isolate transistors from the substrate, which results in lower parasitic capacitance and reduced junction leakage. Combining SOI substrates with strained Si technology takes advantage of the performance enhancement by both SOI on the one hand and the increased carrier mobility of strained Si on the other hand. Typically, the method of choice to obtain Ge-free sSOI is to transfer strained Si grown on a relaxed $Si_{1-x}Ge_x$ buffer layer onto an oxide layer using SMART CUT™ technology [31] that employs a combination of hydrogen ion implantation and wafer

bonding technology [32]. The built-in strain level can be modulated by selectively choosing the Ge doping content of $Si_{1-x}Ge_x$.

The samples used in this study consist of a 60 nm-thick sSOI epilayer built on 145 nm-thick buried oxide above a 525 μm-thick Si(001) wafer (Figure 10.9a). The necessary unstrained reference position has been generated by milling a trench with nominal dimensions of 350 μm × 350 μm × 500 nm using a dual-source ion column sputter gun (thermal ionization Cesium source, three-lens ion column) at a beam energy of 2 keV. The trench is characterized by gently inclined sidewalls and a smooth bottom that is the result of the comparatively low incident angle of 45° and the absence of differential sputtering along this particular incoming direction. However, the most important characteristic is the extremely thin amorphization layer (≈3 nm) on top of the silicon substrate caused by the ion–solid interaction that allows high-resolution diffraction patterns to be captured (Figure 10.10). The EBSD measurements were made using a Zeiss Crossbeam® 1540 EsB at beam energies of 10 keV, 20 keV, and 30 keV and a beam current of ∼8 nA. All EBSPs have been recorded at full resolution (1344×1024 pixel^2, frame averaging over 10 frames) utilizing a NordlysI camera and a Channel5 software suite. Figure 10.9a illustrates the Cartesian axes system that has been used to describe the strain and rotation tensor: x_1 along the $[110]_{Si}$ direction, x_2 along the $[1\bar{1}0]_{Si}$ direction, and x_3 along the wafer surface normal, that is, $[001]_{Si}$. Strains and rotations have been determined using the method described by Wilkinson *et al.* [18].

Linescans have been conducted on the surface of the sSOI layer ranging from the center of the milled trench to a position 700 μm away from the reference position. The quality of the individual measurements along the linescans has been measured using a pattern quality parameter and the normalized cross-correlation peak height proposed in Ref. [25] (Figure 10.10). As expected, both parameters evidence a significant reduction in data quality at the sidewalls of the trench where noncrystalline oxide is exposed to the sample surface. In order to avoid misinterpretation of strains and rotations at these positions, the data sets have been filtered using
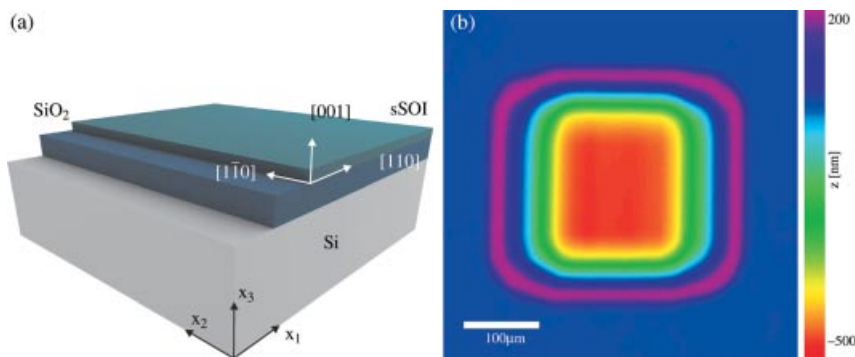

Figure 10.9 (a) Reference axes used for the analysis of the strained Silicon-on-Insulator system and (b) white light interferometer image of the trench that has been milled in order to provide an unstrained reference position.
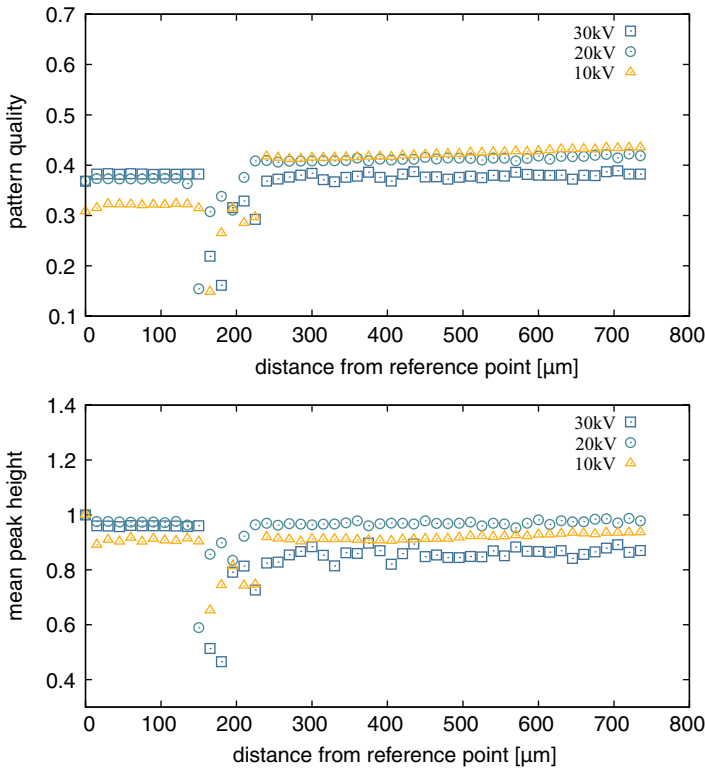
Figure 10.10 (a) Image quality and (b) mean cross-correlation peak height parameter.

threshold values for these two parameters. Furthermore, Figure 10.10 illustrates differences in pattern quality for the three beam energies as well as between the silicon substrate and the sSOI. In particular in case of 10 keV beam energy, the measured pattern quality of the unstrained reference area is significantly decreased. It is reasonable to assume a noticeable influence of the thin amorphization layer above the silicon substrate on the pattern quality, especially for EBSPs obtained from shallow penetration depths. In contrast, the distribution of pattern quality in case of 30 keV beam energy shows no significant difference between trench bottom and strained layer but a larger variation of pattern quality in the area of sSOI that might be caused by defects at higher depths or be influenced by the underlying oxide.

Figure 10.11 shows the distribution of each of the strain components along the linescan. The experimental results confirm the expected biaxial strain state of the sSOI, which is evidenced by a tensile strain ε_{11} and ε_{22}, respectively. Furthermore, ε_{33} takes compressive values in order to maintain the imposed σ_{33} equals zero condition. According to the sample symmetry, neither significant differences in shear strains nor rotations are observed. The averaged strain sensitivity measured by the standard deviation is $\sim 3 \times 10^{-4}$ in case of experiments using 10 kV and 20 kV beam energy and 5×10^{-4} for 30 kV. This result is in good accordance with previous assessments
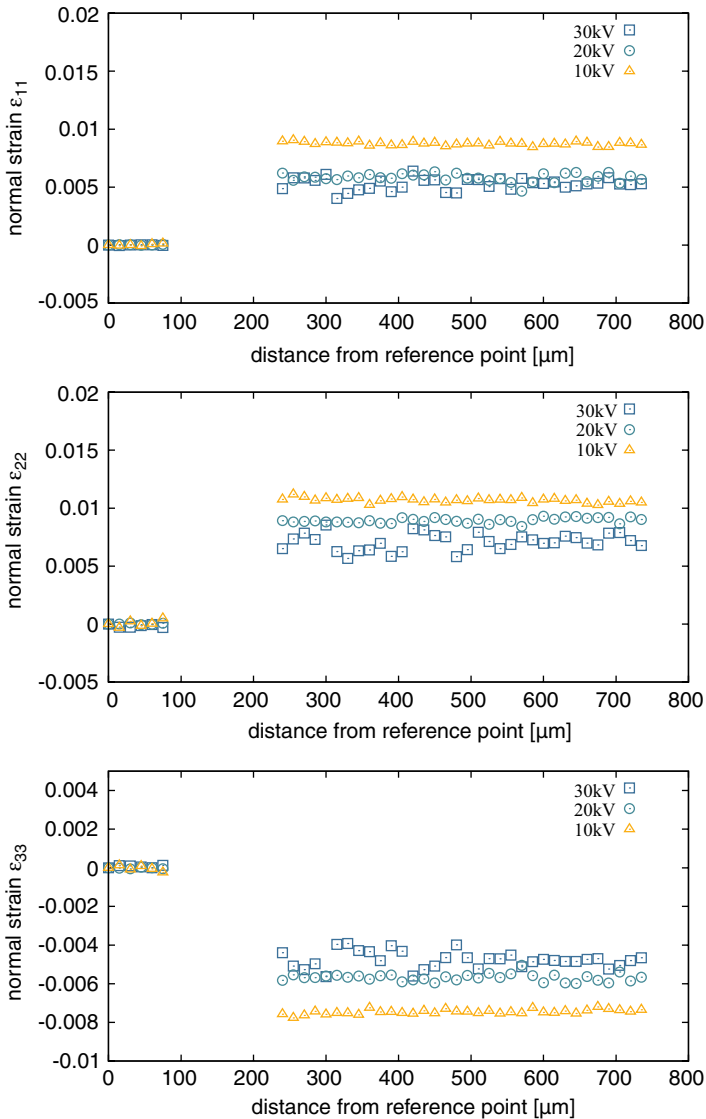
Figure 10.11 Distribution of normal strains along the linescan.

of the sensitivity. Comparison of pattern quality and variations in measured strains demonstrates the direct correlation between both quantities that is also reflected using the mean cross-correlation peak height parameter. However, blurring of patterns obtained from the reference position using a 10 kV electron beam could not be measured using the cross-correlation peak height parameter. This is due to the invariance of the cross correlation to changes in image amplitude, such as those

caused by pattern blurring. For that reason, it seems to be useful to assess the quality of the produced data using both parameters.

10.8
Conclusions

The automated analysis of electron backscatter diffraction patterns has developed into a mature technique to characterize crystalline materials at the subgrain-size level. During the past decade, there have been major efforts to improve the angular resolution of the technique that have opened up an entire new field of applications: local strain measurements with a spatial resolution on the order of 50 nm and high sensitivity of $\sim 10^{-4}$. In particular, the cross-correlation-based pattern analysis, which is also commercially available[2], enables elastic strain tensor measurements at the nanoscale level. Due to the need of an unstrained reference position and high-quality patterns, this methodology can be used for strain determination in silicon devices that are fundamental for a multitude of microelectronic devices and MEMS technology. In this case, the necessary reference position could be provided by either choosing a measurement position far away from the strained sample region or by using sophisticated target preparation techniques. Especially, the use of low-energy sputtering combined with sequential chemical analysis (i.e., AES, XPS, or TOF-SIMS) seems to be a promising tool to locally remove different types of material in order to reveal the unstrained silicon substrate and to measure the displacement gradient tensor of strained silicon or SiGe. More recently, the use of simulated reference patterns has been discussed controversially within the EBSD community [24, 33, 34]. This approach relies on an iterative procedure that is used to minimize the distortion between experimental patterns and patterns simulated at the deformed state in order to reflect the strain state of the experimental EBSPs. Due to the inherent poor accuracy of Hough-based source position determination, significant errors could be expected that are unavoidable using standard calibration routines. Even the use of novel, more accurate methods [35] might not attain the precision required to use this methodology. Despite this, a continuous progress in the development of EBSD for strain determination could be stated, ranging from new analysis routines and sampling strategies to avoidance of errors and novel fields of application.

2) CrossCourt 3 software from BLG Productions, Bristol, UK (www.blgproductions.co.uk).

References

1 Adams, B.L., Wright, S.I., and Kunze, K. (1993) Orientation imaging: the emergence of a new microscopy. *Metall. Trans. A*, **24A**, 819–831.

2 Bastos, A., Zaefferer, S., and Raabe, D. (2008) 3-Dimensional EBSD study on the relationship between triple junctions and columnar grains in electrodeposited Co–Ni films. *J. Microsc.*, **230**, 487–498.

3 Sivakov, V.A., Broenstrup, G., Pecz, B., Berger, A., Radnoczi, G.Z., Krause, M., and Christiansen, S. (2010) Realization of vertical and zigzag single crystalline silicon nanowire architectures. *J. Phys. Chem. C*, **114**, 3798–3803.

4 Baba-Kishi, K.Z. and Dingley, D.J. (1989) Backscatter Kikuchi diffraction in the SEM for identification of crystallographic point groups. *Scanning*, **11**, 305–312.

5 Dingley, D.J. and Wright, S.I. (2009) Phase identification through symmetry determination in EBSD patterns, in *Electron Backscatter Diffraction in Materials Science*, Springer Science + Business Media, LLC, pp. 97–107.

6 Krause, M., Maerz, B., Bennemann, S., and Petzold, M. (2010) High resolution analysis of intermetallic compounds in microelectronic interconnects using electron backscatter diffraction and transmission electron microscopy. Proceedings IEEE 60th Electronic Components and Technology Conference (ECTC 2010), pp. 591–598.

7 Winkelmann, A. (2008) Dynamical effects of anisotropic inelastic scattering in electron backscatter diffraction. *Ultramicroscopy*, **108**, 1546–1550.

8 Winkelmann, A. (2009) Dynamical simulation of electron backscatter diffraction patterns, in *Electron Backscatter Diffraction in Materials Science*, Springer Science + Business Media, LLC, pp. 21–33.

9 Winkelmann, A. and Nolze, G. (2010) Analysis of Kikuchi band contrast reversal in electron backscatter diffraction patterns of silicon. *Ultramicroscopy*, **110**, 190–194.

10 Winkelmann, A., Trager-Cowan, C., Sweeney, F., Day, A.P., and Parbrook, P. (2007) Many-beam dynamical simulation of electron backscatter diffraction patterns. *Ultramicroscopy*, **107**, 414–421.

11 Randle, V. and Engler, O. (2000) *Texture Analysis: Macrotexture, Microtexture and Orientation Mapping*, CRC Press.

12 Wilkinson, A.J. (2000) Measuring strains using electron backscatter diffraction, in *Electron Backscatter Diffraction in Materials Science*, Kluwer Academic/Plenum Publishers, pp. 231–246.

13 Maurice, C. and Fortunier, R. (2008) A 3d Hough transform for indexing EBSD and Kossel patterns. *J. Microsc.*, **230**, 520–529.

14 Keller, R.R., Roshko, A., Geiss, R.H., Bertness, K.A., and Quinn, T.P. (2004) EBSD measurement of strains in GaAs due to oxidation of buried AlGaAs layers. *Microelectron. Eng.*, **75**, 96–102.

15 Luo, J.F., Ji, Y., Zhong, T.X., Zhang, Y.Q., Wang, J.Z., Liu, J.P., Niu, N.H., Han, J., Guo, X., and Shen, J.D. (2006) EBSD measurements of elastic strain fields in a GaN/sapphire structure. *Microelectron. Reliab.*, **46**, 178–182.

16 Troost, K.Z., van der Sluis, P., and Gravesteijn, D.J. (1993) Microscale elastic strain determination by backscatter Kikuchi diffraction in the scanning electron microscope. *Appl. Phys. Lett.*, **62**, 1110–1112.

17 Wilkinson, A.J. (1996) Measurement of elastic strains and small lattice rotations using electron backscatter diffraction. *Ultramicroscopy*, **62**, 237–247.

18 Wilkinson, A.J., Meaden, G., and Dingley, D.J. (2006) High-resolution elastic strain measurement from electron backscatter diffraction patterns: new levels of sensitivity. *Ultramicroscopy*, **106**, 307–313.

19 Wilkinson, A.J., Meaden, G., and Dingley, D.J. (2006) High resolution mapping of strains and rotations using electron backscatter diffraction. *Mater. Sci. Tech. Ser.*, **22**, 1271–1278.

20 Dost, M., Kieselstein, E., and Erb, R. (2002) Displacement analysis by means of gray scale correlation at digitised images and image sequence evaluation for micro- and nanoscale applications. *Micromater. Nanomater.*, **1**, 30–35.

21 Villert, S., Maurice, C., Wyon, C., and Fortunier, R. (2009) Accuracy assessment of elastic strain measurement by EBSD. *J. Microscopy*, **233**, 290–301.

22 Britton, T.B., Maurice, C., Fortunier, R., Driver, J.H., Day, A.P., Meaden, G., Dingley, D.J., Mingard, K., and Wilkinson, A.J. (2010) Factors affecting the accuracy of high resolution electron backscatter diffraction when using simulated patterns. *Ultramicroscopy*, **110**, 1443–1453.

23 Krause, M., Graff, A., and Altmann, F. (2010) Strain determination using electron backscatter diffraction. Proceedings 11th International Workshop on Stress-Induced Phenomena in Metallization.

24 Kacher, J., Landon, C., Adams, B.L., and Fullwood, D. (2009) Bragg's law diffraction simulations for electron backscatter diffraction analysis. *Ultramicroscopy*, **109**, 1148–1156.

25 Wilkinson, A.J., Dingley, D.J., and Meaden, G. (2009) Strain mapping using electron backscatter diffraction, in *Electron Backscatter Diffraction in Materials Science*, Springer Science + Business Media, LLC, pp. 231–249.

26 Humphreys, F.J., Huang, Y., Brough, I., and Harris, C. (1999) Electron backscatter diffraction of grain and subgrain structures: resolution considerations. *J. Microscopy*, **195**, 212–216.

27 Zaefferer, S. (2007) On the formation mechanisms, spatial resolution and intensity of backscatter Kikuchi patterns. *Ultramicroscopy*, **107**, 254–266.

28 Krieger Lassen, N.C., Juul Jensen, D., and Conradsen, K. (1994) Automatic recognition of deformed and recrystallized regions in partly recrystallized samples using electron back scattering patterns. *Mater. Sci. Forum*, **157–162**, 149–158.

29 Landon, C.D., Adams, B.L., and Kacher, J. (2008) High-resolution methods for characterizing mesoscale dislocation structures. *J. Eng. Mater. Technol. ASME*, **130**, 021004.

30 Miyamoto, G., Shibata, A., Maki, T., and Furuhara, T. (2007) Precise measurement of accommodation strain in austenite surrounding martensite by electron backscatter diffraction. Proceedings 1st International Symposium on Steel Science, The Iron & Steel Institute, Japan.

31 Bruel, M., Aspar, B., and Auberton-Herve, A.J. (1997) Smart-cut: a new silicon on insulator material technology based on hydrogen implantation and wafer bonding. *Jpn. J. Appl. Phys.*, **36**, 1636–1641.

32 Christiansen, S.H., Singh, R., Radu, I., Reiche, M., Gösele, U., Webb, D., Bukalo, S., and Dietrich, B. (2005) Strained silicon on insulator (SSOI) by wafer bonding. *Mater. Sci. Semicond. Process.*, **8**, 197–202.

33 Kacher, J., Basinger, J., Adams, B.L., and Fullwood, D.T. (2010) Reply to comment by Maurice *et al.* in response to "Bragg's law diffraction simulations for electron backscatter diffraction analysis." *Ultramicroscopy*, **110**, 760–762.

34 Maurice, C., Fortunier, R., Driver, J., Day, A., Mingard, K., and Meaden, G. (2010) Comments on the paper "Bragg's law diffraction simulations for electron backscatter diffraction analysis" by Josh Kacher, Colin Landon, Brent L. Adams & David Fullwood. *Ultramicroscopy*, **110**, 758–759.

35 Maurice, C., Dzieciol, K., and Fortunier, R. (2011) A method for accurate localisation of EBSD pattern centres. *Ultramicroscopy*, **111**, 140–148.